


---

This is the **accepted version** of the journal article:

Guster, Bogdan; Pruneda, Miguel; Ordejon, Pablo; [et al.]. «Anion ordering transition and Fermi surface electron-hole instabilities in the (TMTSF)<sub>2</sub>ClO<sub>4</sub> and (TMTSF)<sub>2</sub>NO<sub>3</sub> Bechgaard salts analyzed through the first-principles Lindhard response function». *Journal of Physics Condensed Matter*, Vol. 33, issue 8 (Feb. 2021), art. 85705. DOI 10.1088/1361-648X/abc406

---

This version is available at <https://ddd.uab.cat/record/282553>

under the terms of the  <sup>IN</sup> COPYRIGHT license

# Anion ordering transition and Fermi surface electron-hole instabilities in the $(\text{TMTSF})_2\text{ClO}_4$ and $(\text{TMTSF})_2\text{NO}_3$ Bechgaard salts analyzed through the first-principles Lindhard response function

Bogdan Guster<sup>1</sup>, Miguel Pruneda<sup>1</sup>, Pablo Ordejón<sup>1</sup>, Enric Canadell<sup>2</sup>, Jean-Paul Pouget<sup>3</sup>

<sup>1</sup>Catalan Institute of Nanoscience and Nanotechnology (ICN2), CSIC and The Barcelona Institute of Science and Technology, Campus Bellaterra, 08193 Barcelona, Spain

<sup>2</sup>Institut de Ciència de Materials de Barcelona (ICMAB-CSIC), Campus Bellaterra, 08193 Bellaterra, Spain

<sup>3</sup>Laboratoire de Physique des Solides, CNRS UMR 8502, Université de Paris-Sud, Université Paris-Saclay, 91405 Orsay, France

**Abstract.** The first-principles electron-hole Lindhard response function has been calculated and analyzed in detail for two  $(\text{TMTSF})_2\text{X}$  ( $\text{X} = \text{ClO}_4$  and  $\text{NO}_3$ ) Bechgaard salts undergoing different anion-ordering (AO) transitions. The calculation was carried out using the real triclinic low-temperature structures. The evolution of the electron-hole response with temperature for both relaxed and quenched salts is discussed. It is shown that the  $2k_F$  response of the quenched samples of both salts display a low temperature curved and tilted triangular continuum of maxima. This is not the case for the relaxed samples.  $(\text{TMTSF})_2\text{ClO}_4$  in the AO state exhibits a more quasi-1D response than in the non AO state and relaxed  $(\text{TMTSF})_2\text{NO}_3$  shows a sharp maximum. The curved triangular plateau of the quenched samples results from multiple nesting of the warped quasi-1D Fermi surface which implies the existence of a large  $q$  range of electron-hole fluctuations. This broad maxima region is around 1 % of the Brillouin zone area for the  $\text{X} = \text{ClO}_4$  salt (and  $\text{X} = \text{PF}_6$ ) but only 0.1 % for the  $\text{X} = \text{NO}_3$  salt. It is suggested that the strong reduction of associated SDW fluctuations could explain the non detection of the SDW-mediated superconductivity in  $(\text{TMTSF})_2\text{NO}_3$ . The calculated maxima of the Lindhard response nicely account for the modulation wave vector experimentally determined by NMR in the SDW ground state of the two salts. The critical AO wave vector for both salts is located in regions where the Lindhard response is a minimum so that they are unrelated to any electron-hole instability. The present first-principles calculation reveals 3D effects in the Lindhard response of the two salts at low temperature which are considerably more difficult to model in analytical approaches.

*Keywords:* Bechgaard salts, anion ordering, spin density waves, density functional theory, Lindhard response function.

## 1. Introduction

Since the synthesis of the Fabre [(TMTTF)<sub>2</sub>X] and Bechgaard [(TMTSF)<sub>2</sub>X] salts at the end of the 1970s (TMTTF is tetramethyltetrafulvalene, TMTSF is tetramethyltetraselenafulvalene and X is a monovalent anion such as PF<sub>6</sub><sup>-</sup>, ClO<sub>4</sub><sup>-</sup> and NO<sub>3</sub><sup>-</sup>), a lot of attention has been devoted to the establishment of the complex phase diagram of these prototypical quasi-one dimensional (1D) quarter-filled organic salts [1, 2]. The competition between numerous ground states resulting from the coupling of charge, spin and structural degrees of freedom are at the origin of the longstanding interest on these paradigmatic low-dimensional correlated materials. Basically, the physics of the Fabre and Bechgaard salts is governed by the interplay of electron-electron repulsions and inter-stack interactions which are very anisotropic. The former are dominant in the (TMTTF)<sub>2</sub>X series inducing a Luttinger liquid physics, charge localization phenomena and spin-charge decoupling. These two types of interaction compete in the (TMTSF)<sub>2</sub>X series so that a progressive deconfinement of carriers to neighboring stacks as well as an associated dimensional crossover is induced upon cooling: first from 1D to 2D and then to 3D [3]. At high temperature (TMTSF)<sub>2</sub>X behaves as a collection of uncoupled 1D Luttinger liquids located in the stack direction (*a*), then at low temperature as a 2D Fermi liquid located in the (*a*,*b*) donor layers which is subject to a spin density wave (SDW) instability and, finally as a 3D Fermi liquid which is subject to superconductivity [4], when the delocalization along the inter-layer direction *c*\* becomes thermally relevant.

The 1D-2D electronic crossover is revealed by the thermal dependence of the electron-hole response. For a layer of chains coupled by *t*<sub>⊥</sub> the electron-hole response continuously evolves upon cooling from the response of a 1D metal (1D Luttinger liquid in case of sizeable electron-electron interactions), above *T*<sub>U</sub>, to the response of a 2D metal, below *T*<sub>L</sub> [5]. For a free electron gas: *T*<sub>U</sub> = 2*t*<sub>⊥</sub> and *T*<sub>L</sub> = *t*<sub>⊥</sub>/π. In the presence of electron-electron repulsions *t*<sub>⊥</sub> are downward re-normalized and *T*<sub>U</sub> and *T*<sub>L</sub> are smaller [3, 5]. The continuous crossover from *T*<sub>U</sub> to *T*<sub>L</sub> is clearly revealed by the *q* dependence of the first-principles Lindhard response of (TMTSF)<sub>2</sub>PF<sub>6</sub> [6] (note that DFT calculation neglects electron-electron correlations). As expected, *T*<sub>L</sub> coincides with the

detection of a transverse plasma edge when the electric field is applied in the inter-stack direction *b*' of (TMTSF)<sub>2</sub>PF<sub>6</sub> [7]. The deconfinement from the high temperature 1D Luttinger liquid to a 2D Fermi liquid behavior, which can be probed by the opposite rate of thermal variation of the inter-layer *c*\* conductivity, is curiously found also at about *T*<sub>L</sub> ~ 100 K in (TMTSF)<sub>2</sub>PF<sub>6</sub> [8]. However the study of (TMTSF)<sub>2</sub>ClO<sub>4</sub> suggests that the deconfinement transition occurs at a higher temperature than the 1D-2D dimension crossover. In this salt the opposite rate of variation of the thermal dependence of the *c*\* conductivity suggests an inter-stack deconfinement around room temperature (RT) [9], while polarized reflectance measurements along *b*' do not reveal any evidence of a plasma edge at this temperature [10]. This suggests that the 1D-2D dimension crossover should occur at a lower temperature *T*<sub>L</sub> which can be estimated between 200 K and 100 K from the measurement of the dielectric function for an electric field polarized along *b*' [11]. Finally, the detection of a small Drude component below ~ 10 K in the optical conductivity measured along the inter-layer *c*\* direction of (TMTSF)<sub>2</sub>ClO<sub>4</sub> indicates the occurrence of a low temperature 2D to 3D dimension crossover setting a coherent inter-layer coupling [11].

Below *T*<sub>L</sub> (TMTSF)<sub>2</sub>PF<sub>6</sub> undergoes a metal-insulator transition towards a SDW ground state in the 2D electronic regime at *T*<sub>SDW</sub> = 12 K. (TMTSF)<sub>2</sub>ClO<sub>4</sub> and pressurized (TMTSF)<sub>2</sub>PF<sub>6</sub> become superconducting at *T*<sub>S</sub> ~ 1 K in the 3D electronic regime. There is also accumulating evidence that superconductivity in the Bechgaard salts is achieved by SDW fluctuations [12] whose theoretical treatment relies, in the spirit of quasi-1D physics, upon interference between electron-hole and hole-hole pairing processes [13].

The SDW instability and the SDW phase diagram under pressure and/or magnetic field have been successfully analyzed within the RPA approximation in terms of Fermi surface nesting since more than thirty years [1]. Within this framework the bare electron-hole or Lindhard function is appropriately used. There is however a questionable approximation concerning the modeling of the band structure. Until now the electron-hole instability of the Bechgaard salts has been analyzed via a model electron dispersion based on a pseudo-orthorhombic lattice [1]. It is only recently that the real electron-hole (or Lindhard) response was calculated from first-principles and using

the real triclinic structure of  $(\text{TMTSF})_2\text{PF}_6$  [6]. This calculation showed the occurrence below  $T_U$  of a  $2k_F = a^*/2$  quasi-1D electron-hole instability ( $k_F$  is the Fermi wave vector of the incipient 1D electron gas) which is modulated along  $b^*$  by the inter-stack interaction. However, the  $b^*$  dependence of this electron-hole response varies substantially below  $T_L$  making clear the presence of several competing FS nesting processes. As a consequence, it was found a triangular continuum of maximal response which includes the SDW modulation wave vector experimentally observed below  $T_{SDW}$ . The purpose of the present work is to report and analyze the first-principles electron-hole response for different Bechgaard salts incorporating non-centrosymmetric anions of different shape as  $\text{ClO}_4$  and  $\text{NO}_3$ . An important goal of this work is to examine the impact of their anion ordering (AO) transitions [14] on the electron-hole response. This study is all the more interesting since, below  $T_{AO}$ , the  $\text{X} = \text{NO}_3$  salt keeps the insulating SDW ground state whereas the  $\text{X} = \text{ClO}_4$  salt remains metallic and becomes superconducting [15] although, if samples of the latter are quenched through the AO transition, the ground state changes to a SDW one. Thus, in order to rationalize the phase diagram of the Bechgaard salts and in particular the occurrence of the SDW ground state, it is essential to determine how the AO process modifies the electron-hole Lindhard response.

$(\text{TMTSF})_2\text{ClO}_4$  exhibits a staggered order of the  $\text{ClO}_4^-$  anions in the inter-stack  $b$ -direction below  $T_{AO} = 24$  K [16, 17]. The resulting  $(0, 1/2, 0)$  AO structure is represented in Fig. 1a. However, as mentioned, when samples are slowly cooled through the AO transition,  $(\text{TMTSF})_2\text{ClO}_4$  remains metallic. Upon quenching, which prevents the establishment of the long range anion superstructure below  $T_{AO}$ ,  $(\text{TMTSF})_2\text{ClO}_4$  exhibits a metal-insulator transition towards a SDW ground state at  $T_{SDW} = 6.5$  K (this temperature decreases with the speed of the cooling rate at  $T_{AO}$ ).  $(\text{TMTSF})_2\text{NO}_3$  exhibits a staggered order of the  $\text{NO}_3^-$  anions in the stack  $a$ -direction below about  $T_{AO} = 41\text{-}49$  K [18, 19]. The resulting  $(1/2, 0, 0)$  AO structure is represented in Fig. 1b. When samples are slowly cooled through the AO transition  $(\text{TMTSF})_2\text{NO}_3$  exhibits a SDW ground state at  $T_{SDW} = 9$  K. Note that upon rapid cooling through  $T_{AO}$   $(\text{TMTSF})_2\text{NO}_3$  does not exhibit the  $2a$  AO superstructure [19]. Apparently, the SDW features probed by ESR are independent of the cooling rate of the samples [20]. Although the reconstructed FS due to the AO in the two salts has been the subject of a few recent studies [17, 21, 22, 23] we present here a more quantitative estimation of their nesting properties through the calculation of the first-

principles Lindhard function for both their quenched and AO ground states. Thus, the present study completes our first-principles analysis of the electron-hole response of the Bechgaard salts by considering how the AO interferes with the basic scenario reported in ref. [6].

## 2. Computational details

The DFT calculations [24, 25] were carried out using a numerical atomic orbitals approach, which was developed for efficient calculations in large systems and implemented in the SIESTA code [26, 27]. We have used the generalized gradient approximation (GGA) to DFT and, in particular, the functional of Perdew, Burke and Ernzerhof [28]. Only the valence electrons are considered in the calculation, with the core being replaced by norm-conserving scalar relativistic pseudopotentials [29] factorized in the Kleinman-Bylander form [30]. The non-linear core-valence exchange-correlation scheme [31] was used for all elements. We have used a split-valence double- $\zeta$  basis set including polarization functions [32]. The energy cutoff of the real space integration mesh was 350 Ry. The Brillouin zone (BZ) was sampled with the Monkhorst-Pack scheme [33] using grids of  $(45 \times 45 \times 18)$   $k$ -points to build the charge density. The Lindhard response function,

$$\chi(q) = - \sum_{i,j} \sum_k \frac{f_F(\epsilon_i(k)) - f_F(\epsilon_j(k+q))}{\epsilon_i(k) - \epsilon_j(k+q)}, \quad (1)$$

where  $f_F$  is the Fermi function and  $\epsilon_i(k)$  are the band eigenvalues, was obtained from the computed DFT band eigenvalues  $\epsilon_i(k)$  (i.e. in this work the TMTSF HOMO-based bands of the system). The integral over  $k$ -points of the BZ was approximated by a direct summation over a dense, regular grid of points. As the Lindhard function is more sensitive to the accuracy of the BZ integration than the total energy, especially in very anisotropic systems, and/or in the presence of hot spots in the band structure (e.g. saddle points with the corresponding van Hove singularity in the DOS), the  $k$ -points grid used for its calculation must be more dense than in the standard self-consistent determination of the charge density and Kohn-Sham energy. The calculations are done, nevertheless, using the eigenvalues obtained in the DFT calculation for the coarser grid, and interpolating their values in the denser grid, using a post-processing utility available within the SIESTA package. In this work, for the calculation of the Lindhard response function, the BZ was sampled using a grid of  $(400 \times 400 \times 16)$   $k$ -points. The partially filled bands were those taken into account in the calculations.

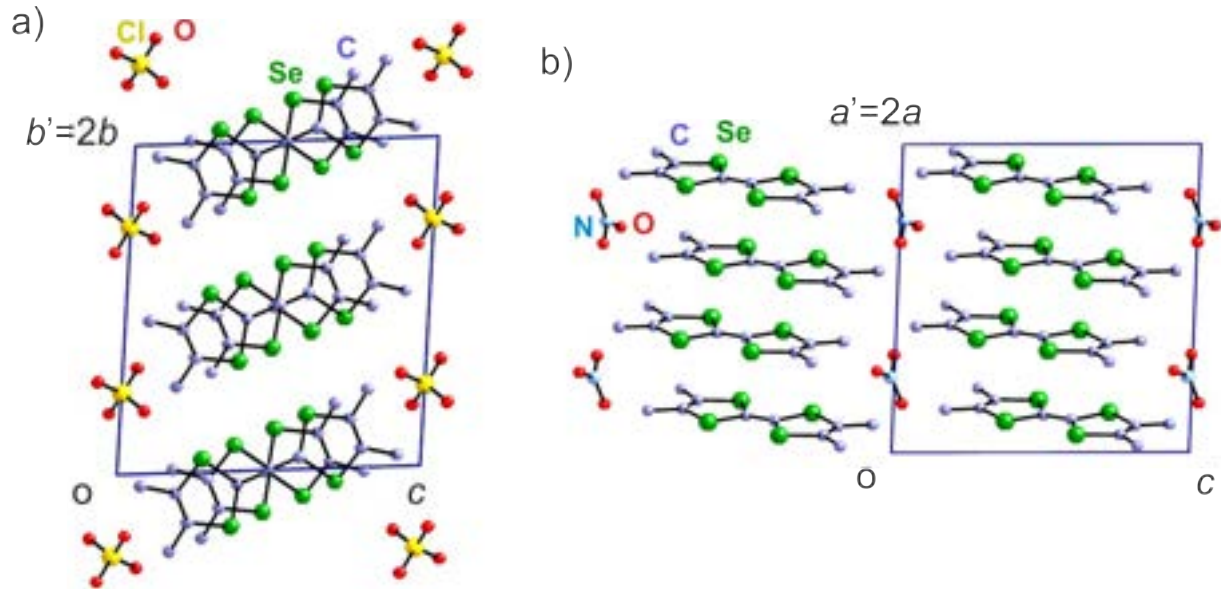


**Figure 1.** (a)  $(0, 1/2, 0)$  anion ordered structure of  $(\text{TMTSF})_2\text{ClO}_4$ . (b)  $(1/2, 0, 0)$  anion ordered structure of  $(\text{TMTSF})_2\text{NO}_3$ . For simplicity hydrogen atoms have not been shown.

Note that the thermal dependencies of the Lindhard functions reported below are due to the Fermi function in Eq. 1. The experimental 7 K average and anion ordered structures of Le Pévelin et al. [17, 34] were used in the calculations for  $(\text{TMTSF})_2\text{ClO}_4$ . The calculations for  $(\text{TMTSF})_2\text{NO}_3$  were based on the 12 K average and anion ordered crystal structures reported by Hebrard-Bracchetti et al. [19, 35]. All values of the Lindhard response are given in units of  $\text{eV}^{-1}$  per crystallographic repeat unit, i.e. one  $(\text{TMTSF})_2\text{X}$  for the structures without AO but two  $(\text{TMTSF})_2\text{X}$  units for the structures with AO. The thermal dependence of the Lindhard responses arises from the thermal factor in the Fermi function  $f_F$ .

The electronic structure of the Bechgaard salts is completely determined by the two pseudo-1D HOMO-based bands. Note that Eq. 1, which has been successfully used to rationalize the physics of these salts [1], is strictly valid for plane waves. In the case of Bloch wave functions each numerator of this equation incorporates the squared matrix element  $|\langle i, k | \exp(iqr) | j, k + q \rangle|^2$  [36]. The matrix element  $|\langle i, k | \exp(iqr) | j, k + q \rangle|^2$  takes into account the spatial overlap of the  $|i, k\rangle$  and  $|j, k + q\rangle$  Bloch functions of bands  $i$  and  $j$  respectively. Recently, there has been some discussion concerning the need to include such matrix elements in the calculation of the response function [37, 38, 39], specially in the context of the puzzling physics of dichalcogenides. As a matter of fact, Eq. 1 should only be used for 1D or pseudo-1D systems. In that case the Fermi surface contains large sheet-like contributions. In addition, these bands (being folded as a result of a weak external potential,

as in the present case, or not) are build from the *same* orbital (the HOMO in the Bechgaard salts [1], the Mo  $d_{xz}$  in the blue bronzes [40]). It is because of the joint occurrence of these two features that the nesting properties of the FS are the driving force for their electronic instabilities and physical behaviour [1]. First-principles calculations for either simple model 1D systems [39] as well as for complex pseudo-1D metallic bronzes like the blue bronzes [40] clearly prove it. Eq. 1 can not be directly used for 2D or 3D systems without caution. In these cases the important bands often result from the hybridization of *different* types of orbitals (the  $d_{z^2}$  and  $d_{x^2-y^2}/d_{xy}$  in NbSe<sub>2</sub> [37], the  $s$ ,  $d_{t_{2g}}$  and  $d_{e_g}$  orbitals in Cr [38]) and consideration of the different matrix elements clearly influences the calculated response [38, 39]. Thus, as in our previous study of the electron-hole response of  $(\text{TMTSF})_2\text{PF}_6$  [6] our first-principles calculations are based on Eq. 1.

### 3. Electronic Structure

The low temperature first-principles electronic structure of  $(\text{TMTSF})_2\text{ClO}_4$  and  $(\text{TMTSF})_2\text{NO}_3$  both in their quenched (without AO) and relaxed (with AO) phases has been discussed recently [22]. However, our previous analysis of the FS of the  $(\text{TMTSF})_2\text{PF}_6$  Bechgaard salt [6] has shown that three different nesting processes occur (see Fig. 2). Two of them mostly nest the zones around the inflection points of the warped lines. Because of the triclinic geometry they are different and since these zones around the inflection points are relatively flat they both lead to a linear segment



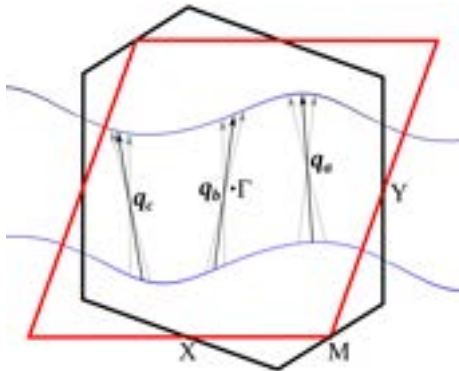


**Figure 2.** Schematic illustration of the three nesting processes occurring in the real Fermi surface of the triclinic Bechgaard salts, which are at the origin of the occurrence of arcs in the Lindhard function (see ref [6] and discussion in section 4).

with high values of the Lindhard function having opposite slopes and different intensities. A third nesting process occurs around the crossing point of these two linear fragments. The occurrence of several FS nesting processes is simply a consequence of the non-regular sinusoidal shape of the FS and consequently, they should be expected for all Bechgaard salts including the present ones before the AO transition (i.e. the quenched samples). However, note that they will certainly differ in subtle details of the warping, a feature that, as it will be discussed in the next section, has strong consequences for their low temperature behaviour. In order to make the link with the calculated Lindhard function discussed in the next sections, we only succinctly discuss here the FS of these salts after the AO transition (i.e. the relaxed samples).

Relaxed  $(\text{TMTSF})_2\text{ClO}_4$  and  $(\text{TMTSF})_2\text{NO}_3$  salts crossing slowly their AO transition double their periodicity along  $b$  and  $a$ , respectively (see Fig. 1). Consequently, their appropriate FS below  $T_{AO}$  basically result from the folding and hybridization of the original (i.e. quenched) FS along  $\pm b^*/2$  and  $\pm a^*/2$ , respectively. Since the folding occurs along different crystallographic directions the calculated FS exhibit different shapes (see Fig. 3). The DFT AO gaps ( $\Delta_0$ ) are calculated to be 14 meV and 8.9 meV for  $(\text{TMTSF})_2\text{ClO}_4$  and  $(\text{TMTSF})_2\text{NO}_3$ , respectively. The different direction of the AO leads to the development of AO gaps at different zones of the original FS, a feature that has important consequences for the physical behavior of these salts below  $T_{AO}$ . For instance the folded FS for  $(\text{TMTSF})_2\text{ClO}_4$  below  $T_{AO}$  is made of two warped planes separated by small AO gaps (band 1 and band 2 in Fig. 3a) which develop at the regions of the original FS with better nesting. Thus, it is expected that AO should exert a considerable influence on the nature of the SDW instability of this Bechgaard salt. In contrast,

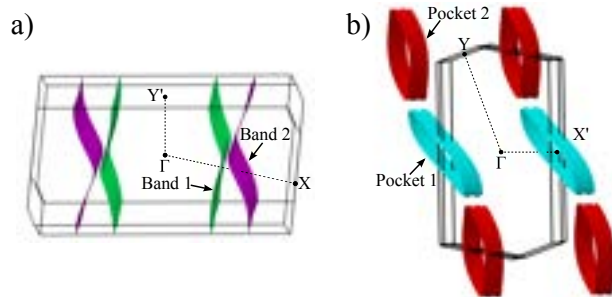


**Figure 3.** Calculated Fermi surface for: (a)  $(\text{TMTSF})_2\text{ClO}_4$  in the  $(0, 1/2, 0)$  AO phase, and (b)  $(\text{TMTSF})_2\text{NO}_3$  in the  $(1/2, 0, 0)$  AO phase. In (a)  $Y'$  refers to  $(0, 1/2, 0)$  in units of the triclinic reciprocal lattice vectors of the  $a \times 2b \times c$  superlattice. In (b)  $X'$  refers to  $(1/2, 0, 0)$  in units of the triclinic reciprocal lattice vectors of the  $2a \times b \times c$  superlattice.

$(\text{TMTSF})_2\text{NO}_3$  becomes a semi-metal below  $T_{AO}$  with a FS made of a series of elongated hole and electron cylinders (pocket 1 and pocket 2 respectively in Fig. 3b) such that the AO gaps develop in regions of the original FS where the nesting is not very good. Thus it is expected that AO should exert a small influence on the nature of the SDW instability of this salt.

## 4. Analysis of the Lindhard function

### 4.1. $(\text{TMTSF})_2\text{ClO}_4$ above $T_{AO}$ as well as in the quenched ground state

Fig. 4 presents selected 2D intensity plots of the Lindhard function of  $(\text{TMTSF})_2\text{ClO}_4$  at 200 K (a), 50 K (c) and 6 K (e) (the latter temperature being close to  $T_{SDW}$  in the quenched structure) in the  $(a^*, b^*)$  reciprocal plane, as well as magnified 3D intensity plots at the same temperatures in the vicinity of the M-X-M Brillouin zone boundary ((b), (d) and (f), respectively). The 200 K plots show that the high temperature response is very anisotropic. The longitudinal scan along  $a^*$  in Fig. 5a shows that the response is sharply peaked at  $0.5a^*$ , corresponding to the  $2k_F$  wave vector of the quasi-1D electron gas. However Figs. 4a and b show that the 200 K response exhibits a significant sinusoidal modulation along  $b^*$ . A more quantitative analysis of the half-width at half-maximum (HWHM) of this modulation (Fig. 6) will be discussed later. The transverse  $b^*$  scan of Fig. 5b also shows that the response exhibits a very broad maximum at the X point which splits into two broad maxima at  $q_0 \approx (0.5, \pm 0.14)$  upon cooling below about 140 K. Also note that two secondary maxima,  $q_2$  and  $q_3$ , which are a bit off the  $2k_F$  line shown in Fig. 5b appear below  $\sim 140$  K and sizeably grow in intensity upon cooling (see Fig. 5b). At 50 K 2D and 3D intensity plots (Figs. 4c and d) show that, due to the presence of these secondary maxima, the Lindhard

response exhibits a curved shape at low temperatures.

Upon cooling the broad curved maximum is progressively transformed into a curved triangular plateau (Figs. 4e and f). The progressive formation of a plateau of maxima is more precisely revealed by the  $q_1$ - $q_2$ ,  $q_2$ - $q_3$  and  $q_1$ - $q_3$  scans of Figs. 7a, b and c respectively (the different  $q_i$  are given in Table. 1. These figures show that the intensity of the  $q_2$  and  $q_3$  peaks reaches the intensity of the  $q_0$  peak around 20 K, temperature below which the curved triangular plateau is well developed. Also Fig. 5a shows that a continuum of intensity with a width of  $\sim 0.02a^*$  develops between  $q_0$  and another  $q_1$  maximum below about 15-20 K (as a consequence the  $b^*$  scan of Fig. 5b exhibits a tilted maximum). The low temperature curved triangular plateau is thus delimited by the  $q_0/q_1$ ,  $q_2$  and  $q_3$  wave vectors already introduced in ref. [6] and indicated in Table 1, as well as in Fig. 7d. At about 15 K, Fig. 7c shows that the maximum of the Lindhard response shifts from  $q_0$  to  $q_3$ . Figs. 4e and f present respectively 2D and 3D intensity plots of the Lindhard response in the  $(a^*, b^*)$  reciprocal plane at  $T_{SDW}$  of the quenched samples (6 K). The intensity of the  $q_0/q_1$ ,  $q_2$  and  $q_3$  responses at 1 K is given in Table 1. As these temperatures are located below  $T_{AO} = 24$  K, the curved triangular shaped Lindhard response is representative of the electron-hole instability of quenched samples.

At temperatures around 15-17 K we also found that the shape of the curved triangular plateau slightly depends of the  $c^*$  component of the Lindhard response. Thus the Lindhard response exhibits a 3D wave vector dependence due to the thermal relevance of the electronic dispersion along  $c^*$ . Fig. 8 gives a superposition of the  $0c^*$  and  $0.5c^*$  cuts of the Lindhard function calculated at 1 K. One observes in particular a splitting along  $b^*$  of the  $q_1$ - $q_3$  line. A similar effect somewhat enhanced is observed in quenched  $(\text{TMTSF})_2\text{NO}_3$ , a feature that will be considered in more detail in Sect. 4.3. However, we did not observe this  $c^*$ -dependence for  $(\text{TMTSF})_2\text{PF}_6$  [6].

Note that in the quenched samples there is a quenched anion disorder so that a distribution of transfer integrals really occurs. *Strictu sensu* this must result with some blurring of the electronic structure and thus some damping of the singularities of the response function. However, even if  $T_{SDW}$  of the quenched  $(\text{TMTSF})_2\text{ClO}_4$  samples (6.5 K) is lower than for  $(\text{TMTSF})_2\text{PF}_6$  (12 K), where there is no anion disorder, the SDW state is not suppressed. Consequently, disorder effects do not strongly alter the nesting features.

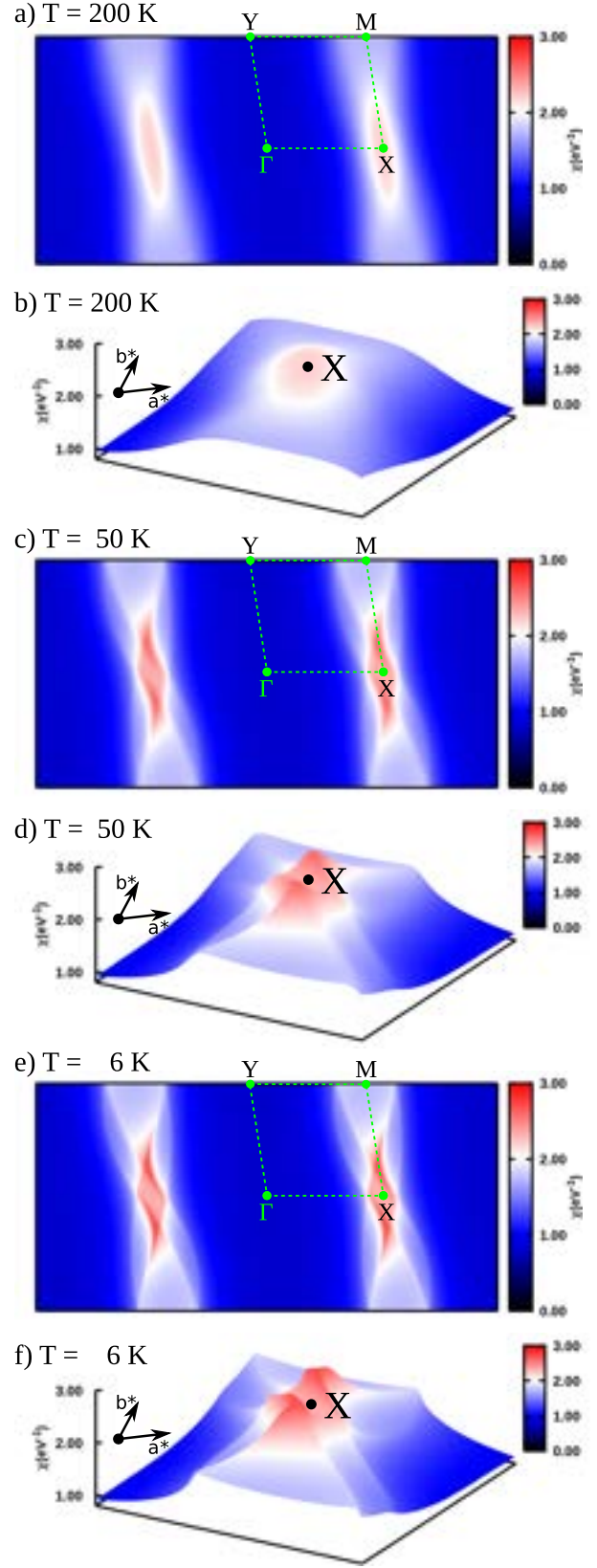


**Figure 4.** 2D plot of the Lindhard function of  $(\text{TMTSF})_2\text{ClO}_4$  in the  $(a^*, b^*)$  reciprocal plane at 200 K (a), 50 K (c) and 6 K (e). 3D sections of the Lindhard function of  $(\text{TMTSF})_2\text{ClO}_4$  around the X-M direction at 200 K (b), 50 K (d) and 6 K (f).

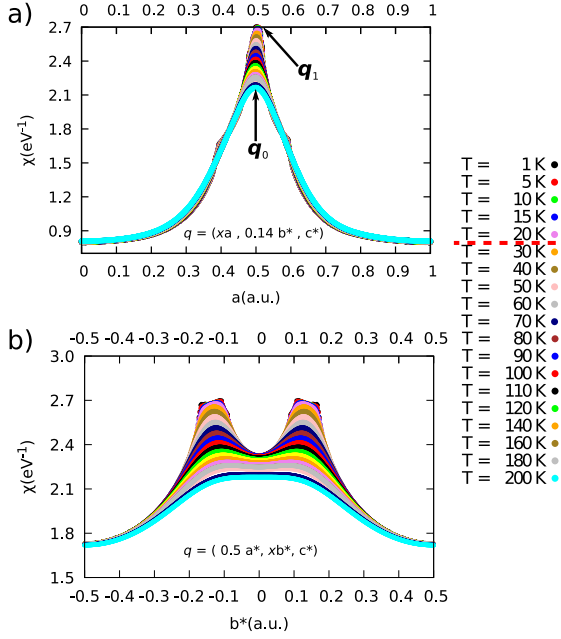


**Figure 5.** Thermal dependence of a longitudinal  $a^*$  scan at  $0.14b^*$  (a) and a transverse  $b^*$  scan at  $0.5a^*$  across the Lindhard function of  $(\text{TMTSF})_2\text{ClO}_4$ . The red dashed line in the temperature scale indicates the temperature at which the single maximum leads to a tilted segment of maxima.

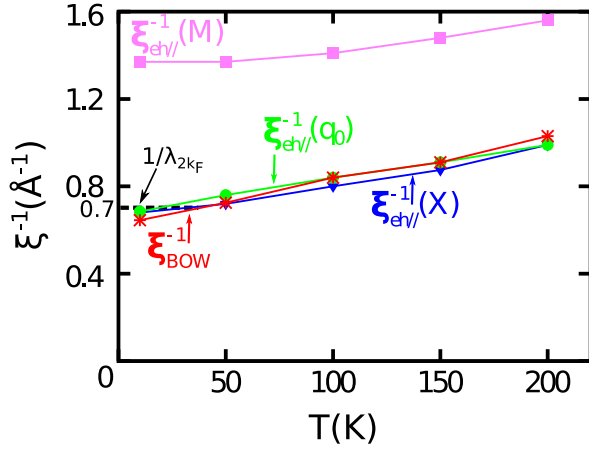


**Figure 6.** Comparison of the thermal dependence of the inverse electron-hole coherence length  $\xi_{eh}^{-1}$  calculated at the  $q_0$ , X and M points with the BOW correlation length  $\xi_{BOW}^{-1}$  of  $(\text{TMTSF})_2\text{ClO}_4$  obtained from the data in ref. [41]

#### 4.2. $(\text{TMTSF})_2\text{ClO}_4$ in the AO phase

Below the  $(0, 1/2, 0)$  AO transition the electronic structure of  $(\text{TMTSF})_2\text{ClO}_4$  is significantly modified since an avoided crossing appears in the Fermi surface, as shown in Fig. 3a. As a consequence, the total Lindhard response in the AO phase represented in Figs. 9a and b for the  $(a^*, b^*)$  plane (with  $b^* = b^*/2$ ) is sizeably modified. However it still exhibits a 1D anisotropy. This response does not vary significantly

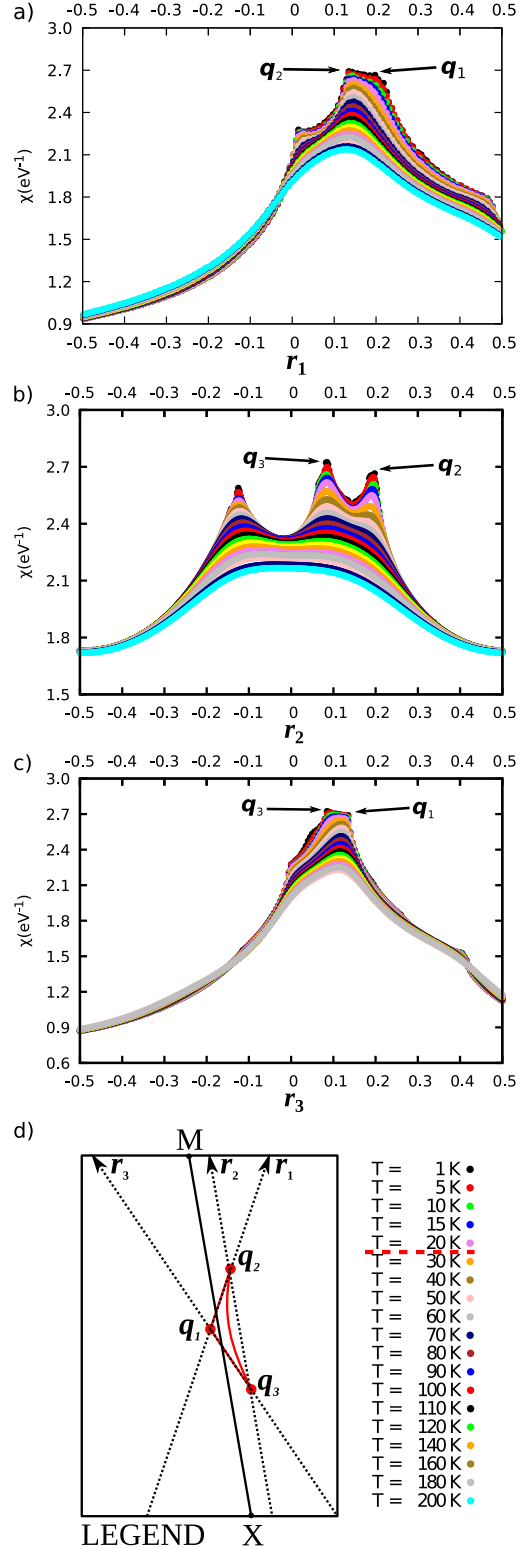


**Figure 7.** Thermal dependence of the scans across:  $q_1$ - $q_2$  (a),  $q_2$ - $q_3$  (b),  $q_3$ - $q_1$  (c) lines of the Lindhard function for quenched  $(\text{TMTSF})_2\text{ClO}_4$ . The red dashed line in the temperature scale indicates the temperature at which the single maximum leads to a tilted segment of maxima. In (d) we present a legend for the scans directions where  $\vec{r}_1 = (1 - \tan(|\vec{q}_1 - \vec{q}_2|))a^* + b^*$ , respectively  $\vec{r}_3 = -(1 + \tan(|\vec{q}_3 - \vec{q}_1|))a^* + b^*$ . Positive values are designated for  $q$  points above the  $\Gamma$ -X direction.



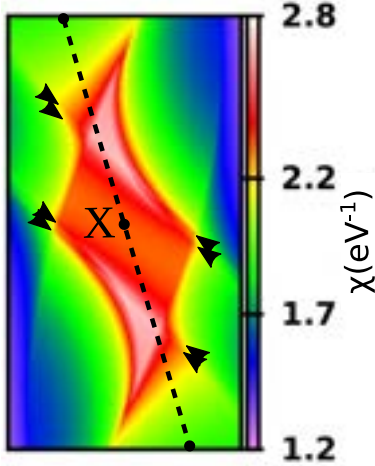


**Figure 8.** Overlap of the Lindhard response function sections for quenched  $(\text{TMTSF})_2\text{ClO}_4$  calculated for planes parallel to  $(a^*, b^*)$  for  $q_{c^*} = 0$  and  $q_{c^*} = 0.5$  at 1 K. Note the black arrows indicating the effect of 3D interactions.

**Table 1.** Location of the  $q_0/q_1$ ,  $q_2$  and  $q_3$  maxima of the low temperature Lindhard response of the  $(\text{TMTSF})_2\text{X}$  Bechgaard salts with  $\text{X} = \text{PF}_6$ ,  $\text{ClO}_4$  and  $\text{NO}_3$ . The table indicates the intensity of these maxima at 1 K. Data for  $\text{X} = \text{PF}_6$  taken from ref. [6].

X	PF6	ClO4	NO3
$q_0$	(0.50,0.23)	(0.50,0.14)	(0.50,0.27)
$q_1$	(0.48,0.23)	(0.48,0.14)	(0.50,0.27)
$\chi_{eh}(q_1)$ [ $\text{eV}^{-1}$ ]	2.66	2.69	2.62
$q_2$	(0.52,0.30)	(0.56,0.21)	(0.52,0.29)
$\chi_{eh}(q_2)$ [ $\text{eV}^{-1}$ ]	2.76	2.65	2.64
$q_3$	(0.53,0.14)	(0.57,0.07)	(0.52,0.24)
$\chi_{eh}(q_3)$ [ $\text{eV}^{-1}$ ]	2.58	2.72	2.54
$T^*$ (onset $q_2, q_3$ )	100 K	140 K	70 K
Fraction of $(a^*, b^*)$ Brillouin zone	0.7 %	1.2 %	0.1 %

between 24 K ( $T_{AO}$ ) and 1 K, temperature at which  $(\text{TMTSF})_2\text{ClO}_4$  becomes a superconductor.

As the Fermi surface contains the contributions of two warped quasi-1D bands (contributions noted band 1 and 2 in Fig. 3a), one should decompose the total Lindhard response into intra-band and interband components as shown in Figs. 9c to e. Each intra-band response (Figs. 9d and e) appears as a pair of contributions slightly split around  $a^*/2$  which are warped and modulated in intensity along  $b^*$ . The inter-band response (Fig. 9c) is more 1D, located at  $a^*/2$  and weakly modulated along  $b^*$ . Figs. 9d and e show that each quasi-1D intra-band response exhibits arcs of intensity maxima. They are located around  $(+0.6, +0.25)$  and  $(+0.4, -0.25)$  reciprocal positions for band 1 and  $(+0.4, -0.15)$  and  $(+0.6, +0.15)$  reciprocal positions for band 2. The 1D inter-band response shown in Fig. 9c is the strongest response and largely determines the shape of the response function.

Figure 10 gives full details about the quasi-1D inter-band response. Figure 10a presents a  $b^*$  scan of this response for  $0.5a^*$ . It exhibits a weak and broad

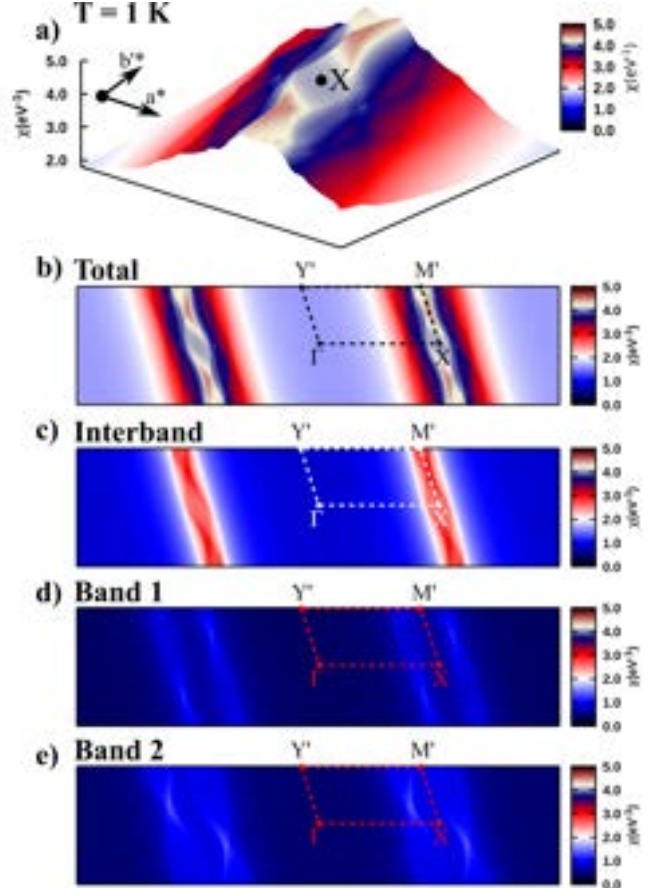


**Figure 9.** 3D plot of the Lindhard function of  $(\text{TMTSF})_2\text{ClO}_4$  in the AO phase at 1 K ( $\sim T_S$ ) (a). 2D plots of the decomposition of this Lindhard function (b) into the inter-band (c), first band (d), and second-band (e) components. The Lindhard function values are given in units of  $\text{eV}^{-1}$  per two  $(\text{TMTSF})_2\text{ClO}_4$  units.

modulation which can be fitted by two Lorentzians centered at  $\pm 0.29b^*$ , whose maximum is close to the  $q_0$  maximum observed above  $T_{AO}$  (remind that  $b^* = 2b^*$ ). Figs. 10b, c and d show different  $a^*$  cuts of this response for  $b^* = 0$  (i.e. through the X point) (b),  $b^* = 0.3$  (c) and  $b^* = 0.5$  (i.e. through the M' point) (d). Figures 10b and d exhibit a truncated broad Lorentzian profile in the scan direction. The saturation of the response between  $0.5 \pm 0.04a^*$  at the X point and  $0.5 \pm 0.03a^*$  at the M' point is due to the fact that the nesting process for these  $q$  wave vectors is stopped by the formation of sizeable pockets which suppress the divergence of the electron-hole response. The HWHM of the underlying Lorentzian profile of  $0.05 \text{ \AA}^{-1}$  leads to an electron-hole coherence length of  $20 \text{ \AA}$ , slightly larger than that found in the non AO phase (Fig. 6). The cut of Fig. 10c around the best nesting wave vector  $(0.5a^*, 0.3b^*)$  shows a more pronounced divergence. This scan reveals also the superposition of the previously described broad component and a weaker and sharper response which saturates at  $0.5$

$\pm 0.015a^*$ . This sharper response represents  $\sim 40\%$  of the intensity of the total response. This intensity is modulated along  $b^*$  (see Fig. 10a). If one assumes that this sharp component has a Lorentzian profile along  $a^*$ , one can estimate from its HWHM of  $0.02 \text{ \AA}^{-1}$  an electron-hole coherence length of  $48 \text{ \AA}$  (i.e.  $\sim 7a$ ). In addition, using the HWHM value of  $\sim 0.045 \text{ \AA}^{-1}$  of each Lorentzian fitting the  $b^*$  scan of Fig. 10b one obtains an electron-hole coherence length of  $22 \text{ \AA}$  along  $b^*$  which is slightly larger than the unit cell parameter ( $b' = 2b = 15.3 \text{ \AA}$ ) of the superstructure. This means that the two nonequivalent chains of the unit cell, between which there is a charge transfer, are consistently coupled by the inter-band nesting mechanism.

#### 4.3. $(\text{TMTSF})_2\text{NO}_3$ above $T_{AO}$ and in the quenched ground state

The shape of the Lindhard function for  $(\text{TMTSF})_2\text{NO}_3$  bears some resemblance with that of  $(\text{TMTSF})_2\text{ClO}_4$  (Sect. 4.1). Figs. 11a and b give respectively the 2D and magnified 3D intensity plots of the Lindhard response at 120 K. As shown in more detail in the scans of Fig. 12a, the Lindhard response is centered at  $2k_F = 0.5a^*$ . The  $b^*$  scan of Fig. 12b makes clear the existence of two broad maxima for  $q_0 = (0.5, \pm 0.27)$  which grow in intensity upon cooling. The shape of the maxima transform into curved arcs below around 70 K. These arcs are defined by the growth of the  $q_2$  and  $q_3$  secondary maxima whose wave vectors are indicated in Table 1. Figs. 11c and d give the 2D and 3D intensity plots of the Lindhard response at 40 K which is close to the anion ordering transition ( $T_{AO} \sim 41\text{-}49 \text{ K}$ ). It is interesting to remark that the  $(1/2, 0, 0)$  AO critical wave vector is located at the X point where the Lindhard response is minimum (see Fig. 11d). Thus the  $(1/2, 0, 0)$  AO is unrelated with any electron-hole instability.

The Lindhard response calculated below  $T_{AO}$  as for instance that shown in Figs. 11e and f, is representative of the response of quenched samples. A well defined tilted plateau with curved triangular shape appears around 15-20 K. A magnified 2D plot of this region as calculated at 1 K is shown in Fig. 13a. Note that because of the tilting of the triangular plateau at these temperatures, the  $q_0$  maxima is located on the side of an asymmetric peak. Also at about 12 K the strongest maxima of the Lindhard response shifts from  $q_0$  to  $q_2$ . The intensity of the maxima of the Lindhard response at 1 K is given in Table 1.

As for the  $(\text{TMTSF})_2\text{ClO}_4$  but not  $(\text{TMTSF})_2\text{PF}_6$ , we have found that at low temperatures the response also depends upon  $c^*$ . In Fig. 13b we plot the overlap of two sections of the Lindhard function, those for the  $q_{c^*}$  components of 0.0 and 0.5. One observes in partic-

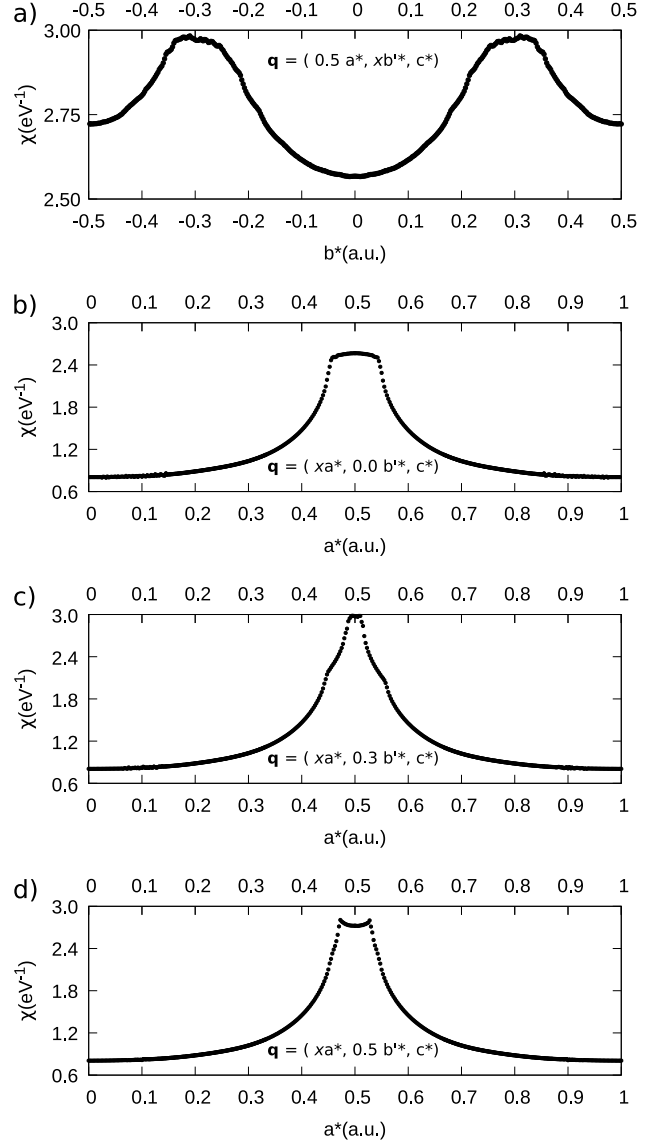


**Figure 10.** Different scans of the inter-band response (in units of  $\text{eV}^{-1}$  per two  $(\text{TMTSF})_2\text{ClO}_4$  units) for  $(\text{TMTSF})_2\text{ClO}_4$  in the AO phase at 1 K. (a)  $b^*$  scan of the response for  $0.5a^*$ . (b)-(d):  $a^*$  cuts of the response for  $0b^*$  (X point) (b),  $0.3b^*$  (c), and  $0.5b^*$  (M' point) (d)

ular a splitting in the region of  $q_3$  marked with black arrows. The inner of these contributions corresponds to the plane with  $q_{c^*} = 0$  and the outer, which is more elongated, to that with  $q_{c^*} = 0.5$ . In the region of  $q_2$  the two contributions remain on top of each other. This change originates from the 3D interactions, i.e. warping of the FS along  $c^*$  in the regions leading to the triangles. This warping varies along the FS and is non negligible for quenched samples in the regions leading to the  $q_3$  nesting but much less in the regions leading to the  $q_2$  nesting. The result is that the region of the triangular plateau around  $q_3$  is spread along the direction of the initial linear component of the arc

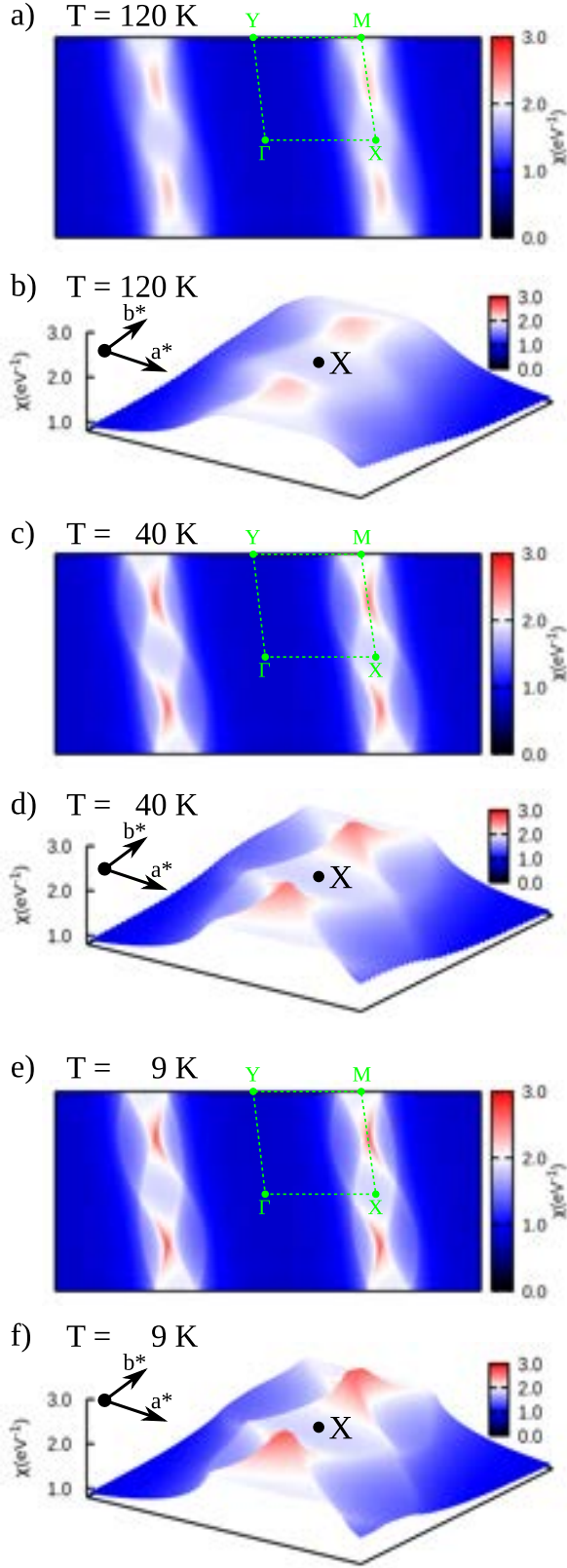


**Figure 11.** 2D plot of the Lindhard function of  $(\text{TMTSF})_2\text{NO}_3$  in the  $(a^*, b^*)$  reciprocal plane at 120 K (a), 40 K (c) and 9 K (e). 3D sections of the Lindhard function of  $(\text{TMTSF})_2\text{NO}_3$  around the X-M direction at 120 K (b), 40 K (d) and 9 K (f).

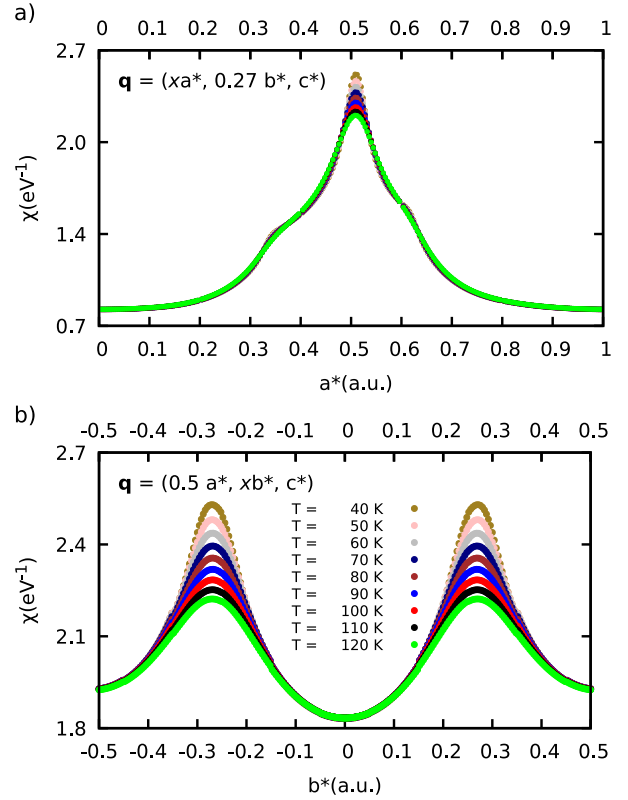


**Figure 12.** Thermal dependence of the transverse  $a^*$  scans across the Lindhard function of  $(\text{TMTSF})_2\text{NO}_3$  at  $0.27b^*$  (a) and  $b^*$  scans at  $0.5a^*$  (b).

whereas that around  $q_2$  does not. Consequently the triangular plateau spreads somewhat in this direction and becomes more inclined. Thus the prevalence of  $q_2$  at low temperature is enhanced by the inter-layer interactions. This effect starts to be visible in our calculations around 12-15 K.

#### 4.4. $(\text{TMTSF})_2\text{NO}_3$ in the AO phase

Below the  $(1/2, 0, 0)$  AO transition the electronic structure of  $(\text{TMTSF})_2\text{NO}_3$  is slightly modified: the periodicity along the donor stacks doubles ( $a' = 2a$ ) so that the donor stacks become weakly tetramerized [19, 35].  $(\text{TMTSF})_2\text{NO}_3$  is a semimetal below  $T_{AO}$  holding an electron pocket (in red in Fig. 3b) and a hole pocket (in blue in Fig. 3b) per unit cell. Thus the Lindhard response in the AO phase should incorporate several components. 2D and 3D plots of the full Lindhard function for this semi-metallic state shown in the  $(a^*, b^*)$  plane (with  $a'^* = a^*/2$ ) are presented in Figs. 14a and b, respectively. This response may be decomposed into the inter-pocket and two intra-pocket components shown in Figs. 14c, d and e respectively. Only the inter-pocket component exhibits a strong response under the form of an intense broad line around  $q_{1D} = 0a'^*$ . The intensity of this  $q_{1D}$  response,

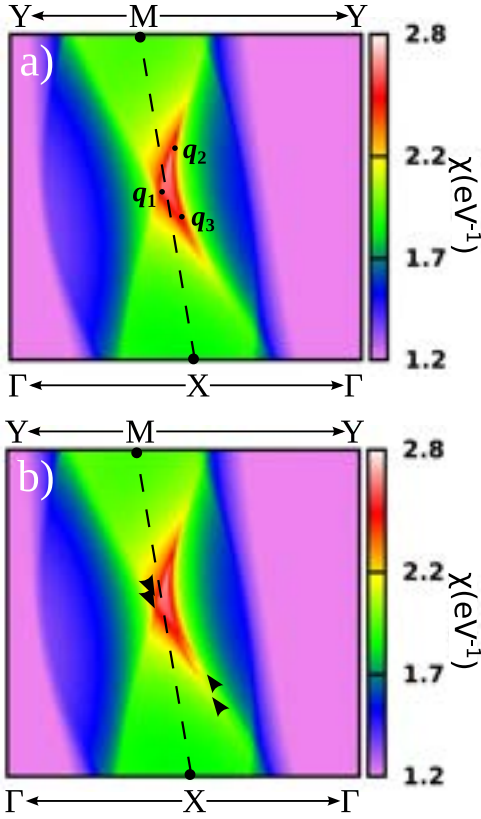


**Figure 13.** (a) Magnified section of the Lindhard function for  $(\text{TMTSF})_2\text{NO}_3$  without AO at 1 K. (b) Overlap of the Lindhard response function sections calculated at planes parallel with  $(a^*, b^*)$  for  $q_{c^*} = 0$  and  $q_{c^*} = 0.5$  at 1 K in the non-ordered phase of  $(\text{TMTSF})_2\text{NO}_3$ . Note the black arrows indicating the effect of 3D interactions.

strongly modulated along  $b^*$ , as shown in Fig. 15, exhibits a maximum at  $0.29b^*$ . A 3D intensity plot of this response at 9 K (i.e. at the  $T_{SDW}$  critical temperature of relaxed samples) is shown in Fig. 16. In contrast with the Lindhard response for quenched samples which exhibited a curved triangular plateau of maxima (Figs. 11 and 13) the Lindhard response in the AO phase exhibits a sharp maximum at  $(0.01, 0.29)$ .

## 5. Discussion

### 5.1. Shape of the Lindhard response above $T_{AO}$ and in the quenched ground state

In the absence of an AO transition, the Lindhard response of  $(\text{TMTSF})_2\text{ClO}_4$  and  $(\text{TMTSF})_2\text{NO}_3$  behaves qualitatively as the  $(\text{TMTSF})_2\text{PF}_6$  one which we analyzed in detail in ref [6]. At high temperature (below  $T_U$  which is above RT) it consists of a quasi-1D response at  $2k_F = 1/2a^*$ , whose intensity is slightly modulated along  $b^*$ . This gives rise to a broad maximum at a  $q_0$  whose  $b^*$  component depends upon the anion (see table 1). This component increases

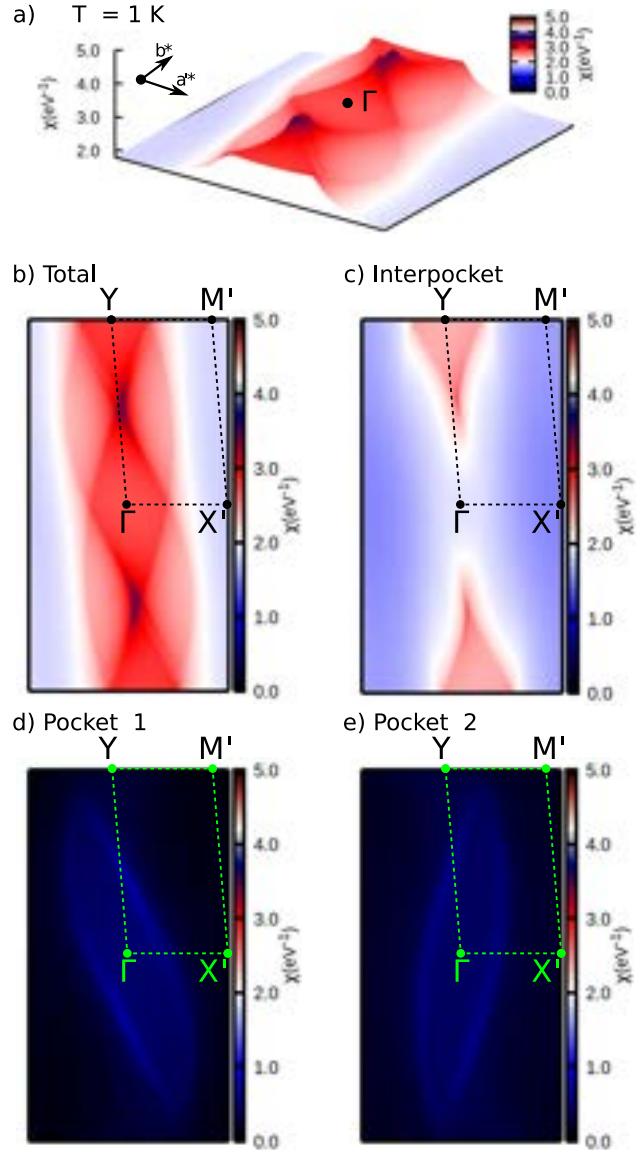


**Figure 14.** 3D plot of the Lindhard response of  $(\text{TMTSF})_2\text{NO}_3$  in its AO phase at 1 K ( $T_{SDW}$ ) (a). 2D plots of the decomposition of this Lindhard function (b) into its inter-pocket (c), pocket 1 (d) and pocket 2 (e) components. See Fig. 3b. The Lindhard function values are given in units of  $\text{eV}^{-1}$  per two  $(\text{TMTSF})_2\text{NO}_3$  units.

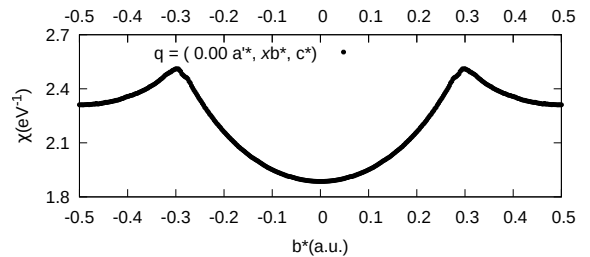


**Figure 15.** Scan of the inter-pocket response of  $(\text{TMTSF})_2\text{NO}_3$  in its AO phase along  $b^*$  (values in units of  $\text{eV}^{-1}$  per two  $(\text{TMTSF})_2\text{NO}_3$  units.).



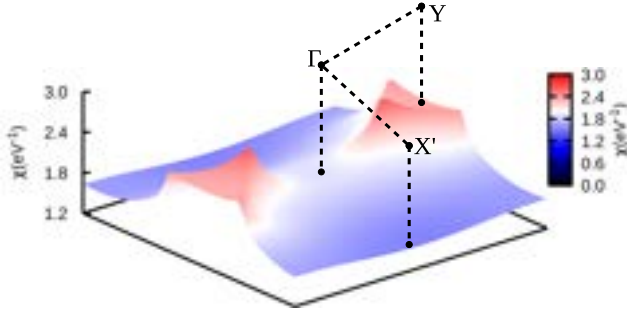


**Figure 16.** 3D plot of the inter-pocket Lindhard function of  $(\text{TMTSF})_2\text{NO}_3$  in its AO phase at 9 K ( $=T_{SDW}$ ). Values given in units of  $\text{eV}^{-1}$  per two  $(\text{TMTSF})_2\text{NO}_3$  units. The maximum response occurs at  $(0.01, 0.29)$ .

substantially from the X =  $\text{ClO}_4$  salt to the  $\text{PF}_6$  salt then to the  $\text{NO}_3$  salt. The shape of the Lindhard response is continuously modified below a temperature  $T^*$  by the development of  $q_2$  and  $q_3$  secondary maxima out of the  $2k_F$  location. As shown in table 1,  $T^*$  decreases from the X =  $\text{ClO}_4$  salt to the  $\text{PF}_6$  salt then to the  $\text{NO}_3$  salt.  $T^*$  apparently coincides with the 1D-2D electronic dimension crossover temperature  $T_L$  at which a transverse plasma edge is detected in the X =  $\text{PF}_6$  [7] and  $\text{ClO}_4$  [11] salts. Upon cooling, the intensity of  $q_2$  and  $q_3$  maxima grow leading to the formation of a boomerang shaped maximum which transforms into a tilted curved triangular region of maxima around 15-20 K (in the quenched state) when the intensity of the  $q_2$  and  $q_3$  maxima become comparable to the  $q_0$  intensity. At about 15 K (in the quenched state)  $q_0$  shifts to  $q_1$  in the X =  $\text{ClO}_4$  salt as previously observed for the  $\text{PF}_6$  salt. There is no sizable shift for the  $\text{NO}_3$  salt.

The area of the  $q_1$ - $q_2$ - $q_3$  low temperature triangular region of maxima per  $(a^*, b^*)$  Brillouin zone is given by

$$\vec{q}_1 \vec{q}_3 \times \vec{q}_1 \vec{q}_2 = f \vec{a}^* \times \vec{b}^*. \quad (2)$$

Such equation defines a fractional occupancy  $f$  which is indicated in table 1.  $f$  is a quantitative measure of the size of the maximal electron-hole fluctuations per Brillouin zone :  $f \sim 1.2$  % for the X =  $\text{ClO}_4$  salt, decreases to  $\sim 0.7$  % for the  $\text{PF}_6$  salt and then to  $\sim 0.1$  %, one order of magnitude smaller, for the  $\text{NO}_3$  salt. These results concern the 2D dispersion of the Lindhard response in the  $(a^*, b^*)$  reciprocal plane. However, note that low temperature calculations reveal that for temperatures around 15 K and below, the Lindhard response is slightly  $c^*$  dependent for the X =  $\text{ClO}_4$  and  $\text{NO}_3$  salts (see Figs. 8 and 13b). However such dependence has not been detected for the Lindhard response of  $(\text{TMTSF})_2\text{PF}_6$  because of the extremely weak band dispersion along the inter-layer  $c^*$ -direction in the region of the Fermi surface nested by the  $q_1$ ,  $q_2$  and  $q_3$  wave vectors. Note that

the  $c^*$  dependence of the Lindhard response for X =  $\text{ClO}_4$  and  $\text{NO}_3$  salts could help fixing the  $q_c$  component of the SDW modulation.

Although at first glance the FS of all Bechgaard salts exhibits quite similar warping along the  $b^*$ -direction, there are in fact subtle differences relying on the magnitude and the phase of the different inter-stack interactions for the different salts. As the  $q_0/q_1$ ,  $q_2$  and  $q_3$  wave vectors (see table 1) correspond to different nesting processes of the FS (Fig. 2), it turns out that the phase of the different FS warping components differs among the salts. In addition, note also that  $T^*$  ( $\approx T_L$ ) below which the  $q_2$  and  $q_3$  nesting processes become thermally relevant, varies among the salts. Consequently, the magnitude of the warping components also varies. Basically, they increase from the X =  $\text{NO}_3$  salt to the  $\text{PF}_6$  salt then to the  $\text{ClO}_4$  salt.

In summary, all indicators qualifying the calculated response of  $(\text{TMTSF})_2\text{PF}_6$  and quenched  $(\text{TMTSF})_2\text{ClO}_4$  and  $(\text{TMTSF})_2\text{NO}_3$ , such as the  $T^*$  onset and the  $f$  fraction, clearly reveal a considerably stronger 1D character of the  $(\text{TMTSF})_2\text{NO}_3$  salt implying weaker inter-stack interactions and a narrower range of 2D SDW fluctuations. As discussed in the next sections we believe that this result is important to understand the peculiar low temperature behavior of this salt

Finally, let us remark that the calculation of the Lindhard response assumes free electrons. Electron-electron repulsions which in 1D systems give rise to a Luttinger liquid type behaviour, are ignored. Strictly speaking the calculation of the Lindhard response should be valid for a Fermi liquid below the deconfinement temperature. As this temperature is around 300 K the calculation is validated for the X =  $\text{ClO}_4$  salt. It could be questionable in the  $\text{PF}_6$  salt where the deconfinement temperature is around 100 K. However since above 100 K the calculated quantities such as the electron-hole coherence length perfectly agree with experimental results [6], one expects that the Lindhard response should be only marginally modified. This is also true for the X =  $\text{NO}_3$  salt where the deconfinement temperature is estimated as  $T^*=70\text{K}$ . However, in this temperature range the physics is perturbed by pretransitional AO fluctuations [18].

### 5.2. Shape of the Lindhard response in the AO ground state

AO changes the electronic band dispersion and the FS of the X =  $\text{ClO}_4$  and  $\text{NO}_3$  salts (see Figs. 3a and b, respectively). As the Lindhard response is very sensitive to the details of the band dispersion in the vicinity of the Fermi energy, the electron-hole



response calculated for the AO phase of these salts should somewhat differ from those calculated above  $T_{AO}$ . For  $(\text{TMTSF})_2\text{NO}_3$  below  $T_{AO}$  both the stack tetramerization and the  $(1/2, 0, 0)$  anion potential perturb the electronic dispersion. As the Lindhard response above and at  $T_{AO}$  is small at the X point (Fig. 12b) one expects a weak response of the stack to the  $(1/2, 0, 0)$  AO potential. Indeed the structural refinement shows that the  $2k_F$ -tetramerization of the stack below  $T_{AO}$  is weak [19]. Because of this observation and the fact that the first-principles calculation leads also to a small value of the AO gap [22], one could argue that the semi-metallic state of  $(\text{TMTSF})_2\text{NO}_3$  should not be so different from the metallic one above  $T_{AO}$ . The total Lindhard response calculated below  $T_{AO}$  (Figs. 14a and b) bears indeed a resemblance with that calculated at  $T_{AO}$  in the non AO structure (Figs. 11c and d) if we take into account the effect of the folding due to the doubling of periodicity along the  $a$ -direction. As mentioned, the Lindhard response of the AO phase is the sum of three components corresponding to the inter-pocket and two intra-pocket nesting processes. The intensity of the inter-pocket Lindhard response, which still exhibits a pronounced quasi-1D anisotropy, is by far the dominant one (Figs. 14c and 15). However, in contrast with the response for quenched samples this response does not exhibit a curved triangular plateau of maxima (Figs. 11e and f) but a sharp peak located at  $(0.01, 0.29)$  in the  $(a^*, b^*)$  reciprocal plane of the  $2a$  superstructure (Fig. 16). Note however that the wave vector position of this peak is quite close to that of the absolute  $q_2$  maximum of the response for quenched samples. Yet when the peak intensity of the maxima are compared,  $1.76 \text{ eV}^{-1}$  per  $(\text{TMTSF})_2\text{NO}_3$  formula unit for the total response in the AO phase vs  $2.64$  for the  $q_2$  maximum (table 1) for the quenched structure, a noticeable decrease of 34 % due to the AO is found. This means that although the anion gap is opened in a region of the FS which is not associated with the best nesting [22], AO has a noticeable effect on the absolute value of the response. In fact although the maximum response is found at practically the same wave vector, the whole response along this value is depleted: the triangular plateau practically disappears and the maximum decreases. The occurrence of these changes are very difficult to appreciate by simple visual inspection of the Fermi surfaces and point out the need for the Lindhard response study for fully understanding the FS nesting properties.

The effect of the AO transition on the electronic structure of  $(\text{TMTSF})_2\text{ClO}_4$  was described in early times as resulting from a simple band folding due to the doubling of the  $b$  periodicity. This situation is in fact more subtle because a shift of the  $\text{ClO}_4$  anions

accompany its ordering, and with the reinforcement of hydrogen bonds with one donor out of two, one stack out of two of the  $2b$  super-cell is substantially deformed [17, 22]. As a consequence, the Lindhard response (Fig. 9) is modified with respect to that of the quenched sample (Figs. 4e and f). Note also that the Lindhard response calculated for the real AO phase differs from the response analytically calculated by the introduction of an anion gap in the band structure [42]. According to the electronic structure of Fig. 3a, the Lindhard response has one inter-band and two intra-band components (Fig. 9). The two intra-band responses are weak, warped and shifted from the average  $\langle 2k_F \rangle = 0.5a^*$  reciprocal position (note that as the two donor stacks of the unit cell are non equivalent there is a charge transfer between them). The inter-band response is the strongest. It has a more 1D type anisotropy than the response of the quenched sample (Figs. 5e and f). Note that even if one could expect that the band splitting due to the AO suppresses the quasi-1D high temperature electron-hole response, our calculation shows that this is not really the case. The intensity maxima per  $(\text{TMTSF})_2\text{ClO}_4$  formula unit for the AO and non AO phases are found to be  $2.24$  and  $2.72 \text{ eV}^{-1}$  so that AO induces a 17 % decrease of the intensity maxima. AO definitely has an effect on the intensity maxima although lower than for the  $(\text{TMTSF})_2\text{ClO}_4$  and, nevertheless, the calculated anion gap is larger,  $\sim 14 \text{ meV}$  vs  $8.9 \text{ meV}$ . The HWHM values of the sharp response lying on top of the broad one of Fig. 10c lead to inverse electron-hole coherence lengths in the stack and inter-stack directions of  $0.024a^*$  and  $0.11b^*$ , respectively. From these values it is estimated that the area of this response is a fraction  $f=2.1\%$  of the area of the Brillouin zone of the superstructure, i.e. a fraction of  $\sim 1 \%$  of the high temperature Brillouin zone area. This value is comparable to the fraction  $f=1.2\%$  calculated for quenched  $(\text{TMTSF})_2\text{ClO}_4$  (see table 1).

In summary, AO brings substantial changes into the Lindhard response of both  $(\text{TMTSF})_2\text{NO}_3$  and  $(\text{TMTSF})_2\text{ClO}_4$ . In both cases the system acquires a stronger 1D character and the intensity maximum of the response decreases. Nevertheless, in contrast with commonly accepted ideas the magnitude of the induced AO gap does not correlate with the decrease of the intensity maximum of the response. The reason is that the wave vector of the AO modulation determines the region of the FS where the gap is going to be opened but this region is not necessarily the region with the better nesting properties. Finally, it is also worth noting that the three components of the Lindhard response of relaxed  $(\text{TMTSF})_2\text{ClO}_4$  bear a resemblance with those of the blue bronze

which undergoes an inter-band charge density wave (CDW)/Peierls transition [40].

### 5.3. Relationship with the SDW ground state

In contrast with AO transitions, the Lindhard response allows to analyze (within the RPA approximation) the SDW modulation observed below  $T_{SDW}$  in quenched  $(\text{TMTSF})_2\text{ClO}_4$  and  $(\text{TMTSF})_2\text{NO}_3$ . In this analysis the SDW modulation wave vector is that bearing an absolute maximum of the Lindhard response. In quenched  $(\text{TMTSF})_2\text{ClO}_4$ , the analysis of the NMR data [43, 44] assuming a  $0.5a^*$  longitudinal component for the SDW modulation, leads to a  $0.12b^*$  transverse modulation component, which is close to the  $q_0 = (0.50, 0.14)$  maximum of the Lindhard response that we find although it is slightly away from the  $q_3 = (0.57, 0.07)$  absolute maximum at  $T_{SDW}$ . The same type of analysis of the NMR data for the AO phase of  $(\text{TMTSF})_2\text{NO}_3$  [45, 46] gives an approximate  $0.25b^*$  transverse modulation component which is close to the position of the single maximum  $(0.01, 0.29)$  of the Lindhard function that we calculate for the  $2a$  superstructure. Note that the NMR modulation wave vector is also close to the  $q_2 = (0.52, 0.29)$  maximum of the Lindhard response in quenched  $(\text{TMTSF})_2\text{NO}_3$ .

The Lindhard response calculation brings also valuable information by showing that quenched samples at low temperature exhibit a triangular plateau of maxima instead of a sharp maximum. This feature implies the existence of a broad region of  $q$  SDW fluctuations which was already discussed in ref. [6] for  $(\text{TMTSF})_2\text{PF}_6$ . This finding can be quantified through the calculated  $q$  area of the plateau which we present in table 1 for the  $X = \text{PF}_6, \text{ClO}_4$  and  $\text{NO}_3$  salts. Basically, there is one order of magnitude difference in this area when comparing the two salts  $X = \text{PF}_6$  and quenched  $X = \text{ClO}_4$  salts with the quenched  $X = \text{NO}_3$  one. This difference qualitatively remains between relaxed  $X = \text{ClO}_4$  and  $\text{NO}_3$  samples. Below we point out that this order of magnitude difference could have some significant consequences if the Cooper pairing mechanism for superconductivity involves SDW fluctuations.

### 5.4. Relationship with the $2k_F$ density wave instability

The scan of the quasi-1D Lindhard response in the  $a$ -direction makes possible to obtain the inverse electron-hole coherence length in the chain direction,  $\xi_{eh}^{-1}$ . Fig. 6 presents thermal variations of this quantity for non relaxed  $(\text{TMTSF})_2\text{ClO}_4$  for several  $b^*$  components. The smallest  $\xi_{eh}^{-1}$  values are obtained for the  $q_0$  and  $X$  points.  $\xi_{eh}^{-1}(q_0)$  of  $(\text{TMTSF})_2\text{ClO}_4$  has a weaker thermal dependence than  $\xi_{eh}^{-1}(q_0)$  of  $(\text{TMTSF})_2\text{PF}_6$  (see Fig. 5 in ref. [6]). Additionally,

in contrast with  $(\text{TMTSF})_2\text{PF}_6$  the inverse electron-hole coherence length  $\xi_{eh}^{-1}(q_0)$  of  $(\text{TMTSF})_2\text{ClO}_4$  becomes comparable to the inverse wavelength  $1/\lambda_{2k_F} = 1/2a$  ( $= 0.07\text{\AA}^{-1}$ ) of the  $2k_F$  fluctuations only below  $\sim 25$  K in the quenched state. Above this temperature the  $2k_F$  fluctuations are thermally incoherent. The  $2k_F$  SDW,  $2k_F$  CDW and  $2k_F$  bond order wave (BOW) fluctuations, whose occurrence can be probed by different experimental techniques depend on the existence of  $2k_F$  electron-hole fluctuations. In fact, three types of  $2k_F$  fluctuations have been detected for  $(\text{TMTSF})_2\text{ClO}_4$ . First, pretransitional  $2k_F$  SDW fluctuations probed by NMR [47] which although enhanced between 30 K and 10 K never become critical (superconductivity is the ground state of relaxed samples). Second, quasi-1D  $2k_F$  BOW fluctuations are detected by X-ray diffuse scattering below 150-200 K [41]. Furthermore, as shown in Fig. 6 the experimental inverse intra-chain correlation length of these fluctuations,  $\xi_{BOW}^{-1}$ , nicely amounts to the calculated inverse electron hole coherence length  $\xi_{eh}^{-1}(q_0)$ . Although detected until low temperature [41, 48], the  $2k_F$  BOW fluctuations, whose  $\xi_{BOW} \approx \xi_{eh}(q_0)$  never exceeds  $\lambda_{2k_F}$ , always remain thermally incoherent. Note that the low temperature growth of  $2k_F$  BOW fluctuations could be inhibited by the onset below 40 K of the  $(0, 1/2, 0)$  AO fluctuations [16]. In this respect, the intensity of  $2k_F$  BOW fluctuations at low temperatures when the  $(0, 1/2, 0)$  AO instability is suppressed is enhanced for  $[(\text{TMTSF})_{1-x}(\text{TMTTF})_x]_2\text{ClO}_4$  alloys when  $x$  increases [48, 49]. Third,  $2k_F$  CDW fluctuations have also been detected by optical means [50].

An intriguing result is that AO  $(\text{TMTSF})_2\text{ClO}_4$  exhibits a  $2k_F$  electron-hole response whose inter-band component shows a pronounced 1D character. At first glance it is thus surprising that superconductivity develops in this phase instead of a  $2k_F$  density wave instability. This is all the more surprising that quenched  $(\text{TMTSF})_2\text{ClO}_4$ , whose Lindhard response has a less pronounced 1D character (see Figs. 11e and f), exhibits a SDW ground state. Another puzzling but related observation is that  $(\text{TMTSF})_2\text{NO}_3$  apparently exhibits a SDW both for AO and non AO samples despite a substantial reduction of the response intensity maxima.  $(\text{TMTSF})_2\text{NO}_3$  is already a very 1D system in the absence of AO as shown by the very small value of  $f$  (0.1). The AO exacerbates such 1D character by transforming the small plateau of the non AO phase into a cusp anomaly in the AO phase so that the SDW formation can be understood even if the maximum response intensity is reduced. Note also that the inter-stack component for both the AO and non AO phases is very near to a commensurate value. The case of  $(\text{TMTSF})_2\text{ClO}_4$  is different because in the non AO

phase there is a very sizeable range of fluctuations ( $f=1.2$ ). Even if the system becomes more 1D, a non negligible range of fluctuations is kept in contrast with the case of the  $(\text{TMTS})_2\text{NO}_3$  salt. It is possible that under such circumstances the decrease of the maximum response intensity brought by the AO is enough to suppress the SDW.

### 5.5. Relationship with the mechanism of superconductivity

When the metallic state is restored by the suppression under pressure of either the insulating SDW or the insulating AO ground states or by slowly crossing the temperature range of the AO transition of the  $\text{X} = \text{ClO}_4$  salt at ambient pressure, Bechgaard salts become superconducting with a  $T_S$  slightly larger than 1 K [15]. The only exception to this observation is pressurized  $(\text{TMTSF})_2\text{NO}_3$ . When the SDW ground state of this salt is removed, superconductivity is not detected down to 50 mK [51]. There is now accumulating experimental evidence that superconductivity of the Bechgaard salts could be mediated by inter-stack attractive SDW fluctuations [4, 12]. One strong argument in favor of such mechanism is that the highest observed  $T_S$  is close to the SDW boundary critical pressure and then when an extra pressure is applied  $T_S$  decreases when SDW fluctuations diminish. Keeping in mind the relevance of quasi-1D physics for the Bechgaard salts, interference between hole-hole superconducting and electron-hole SDW fluctuations should be treated on the same footing. This leads to an attractive SDW mediated  $d$ -wave pairing mechanism between holes located on neighboring stacks [13]. In this context the intensity of the inter-chain exchange mechanism which determines  $T_S$  should necessarily depend upon the importance of  $2k_F$  SDW fluctuations. The amount of such  $2k_F$  SDW fluctuations is related to the  $f$  fraction of the dominant electron-hole  $q$  fluctuations forming the triangular maxima of the Lindhard response described in this work (see table 1). This fraction which is of the order of 0.7% in  $(\text{TMTSF})_2\text{PF}_6$  at ambient pressure does not vary significantly under 7 kbar pressure where SDW and superconductivity coexist (see ref. [6]). For the superconducting AO phase of  $(\text{TMTSF})_2\text{ClO}_4$  we estimate an  $f$  value of 1%, which is the largest among the three salts. These fractions are about one order magnitude larger than that determined in the present study in  $(\text{TMTSF})_2\text{NO}_3$ . It is thus tempting to suggest that the magnitude of SDW fluctuations fixed by the maximum of the electron-hole response of  $(\text{TMTSF})_2\text{NO}_3$  is not important enough to achieve superconductivity above 50 mK. If this scenario is correct the presence of a multi-nested FS should be a prerequisite to promote a large

fraction of electron-hole fluctuations. However since superconductivity results from interference between the Peierls and the Cooper channels this picture is certainly oversimplified. A complete treatment can be found in ref. [13] although the FS used was modelled using the orthorhombic approximation with a single nesting breaking term which according to our work is a simplified representation. Work including a multi-nesting scenario may provide important hints to unravel the superconducting mechanism in Bechgaard salts. Finally, an important output of the present calculation is that the  $2k_F$  electron-hole SDW fluctuations mediating the Cooper appear to be spatially incoherent.

### 5.6. Some comments concerning the $2k_F$ modulated AO transitions

Finally let us remark that the electron-hole Lindhard response could play a role through the electron-anion coupling to settle a response of the organic stack to the anion potential. This should be especially the case when the anion potential is inherently disordered due to the location of non-centrosymmetric anions, such as  $\text{X} = \text{ClO}_4$ ,  $\text{ReO}_4$  and  $\text{NO}_3$ , on inversion centres of the structure. Looking at the coupling of this potential with the electron gas via the Lindhard response thus appears to be a pertinent way to analyse coupled lattice/electronic instabilities involved in AO processes stabilizing the  $2a$  periodicity or  $2k_F$  wavelength *along* the stack direction. In principle, the enhanced electron-hole response at  $2k_F$  could help stabilizing a  $2k_F$  stack modulation as a response to a staggered AO potential as observed for instance for the 180 K  $(1/2, 1/2, 1/2)$  metal-insulator AO transition in  $(\text{TMTSF})_2\text{ReO}_4$  [52, 53]. However, the AO transition of  $(\text{TMTSF})_2\text{ReO}_4$  appears to be more subtle than expected from a simple RPA analysis of the electron-hole response because there is no absolute maximum of the Lindhard function at the M point  $(a^*/2, b^*/2)$ , and no significant low temperature enhancement of the response at M to drive an electron-hole instability (see for example Figs. 5b and 12b). In this particular case the gain of electronic energy due to the gap opening at  $T_{AO}$  following the  $2k_F$  stack bond deformation is achieved through a first order phase transition and not through the second order Peierls one expected from an RPA analysis of the  $q$  dependent response. The  $(1/2, 1/2, 1/2)$  AO transition of  $(\text{TMTSF})_2\text{ReO}_4$  thus seems to be more likely driven by the gain of anions entropy caused by their ordering below  $T_{AO}$ , accompanied by an electronic energy gain caused by a  $2k_F$  stack BOW deformation which follows in a subtle way the staggered AO process via the anion-donor interaction (for more details see ref. [53]). Given the dominant role played by the AO process, the Peierls

mechanism which assumes to be driven by the  $2k_F$  divergence of the electron-hole response and neglects the role of the lattice entropy, cannot be considered as the primary force behind the AO transition. With this ideas in mind the AO transition of  $(\text{TMTSF})_2\text{NO}_3$  provides useful hints concerning the coupling of these instabilities. In this case the anion order-disorder transition is of second order and since the salt becomes a semi-metal at  $T_{AO}$ , no true electronic gap is opened. The  $2k_F$  Lindhard response of  $(\text{TMTSF})_2\text{NO}_3$  does not exhibit an absolute maximum at the X point ( $a^*/2, 0b^*$ ). One can argue that the difference between the X =  $\text{ReO}_4$  and  $\text{NO}_3$  salts may rely on the strength of the electron-anion coupling. The anion-donor coupling through O-Se interactions, reinforced by an anion shift towards the core of the donor in  $(\text{TMTSF})_2\text{ReO}_4$ , is stronger than in  $(\text{TMTSF})_2\text{NO}_3$  where the coupling is achieved through the establishment of hydrogen bonds between the anion and the methyl groups at the periphery of the donor. The presence of a strong anion-donor coupling in  $(\text{TMTSF})_2\text{ReO}_4$  is certainly responsible of the 1st order character of the (1/2, 1/2, 1/2) AO transition (this is a general feature of all Bechgaard salts exhibiting the (1/2, 1/2, 1/2) superstructure [14, 48]). This observation as well as the fact that the calculated Lindhard response never exhibits a maximum for the wave vector of the AO distortion strongly suggests that the AO mechanism of the X =  $\text{ReO}_4$  salt should be interpreted in the framework of a strong coupling theory [54].

## 6. Conclusions

The first-principles Lindhard electron-hole response of the  $(\text{TMTSF})_2\text{X}$  (X =  $\text{ClO}_4$  and  $\text{NO}_3$ ) Bechgaard salts, both in their quenched and relaxed (i.e. AO) ground states, has been calculated using their real triclinic structure. This study, which complements a previous work for  $(\text{TMTSF})_2\text{PF}_6$  [6] which does not undergo an AO transition, shows that despite clear-cut differences the evolution with temperature of the Lindhard response of the three salts has many points in common. In particular the  $2k_F$  response exhibits a low temperature curved and tilted triangular continuum of maxima which implies the existence of a large  $q$  range of electron-hole fluctuations. This broad region of maxima can be explained from the existence of several competing FS nesting processes, a feature that had not been previously reported. This broad maxima amounts to about 1 % of the Brillouin zone area for the X =  $\text{PF}_6$  and  $\text{ClO}_4$  salts and about only 0.1 % for the X =  $\text{NO}_3$  salt. Thus, we suggest that the strong reduction of associated SDW fluctuations when comparing the X =  $\text{PF}_6$  and  $\text{ClO}_4$  salts with the  $\text{NO}_3$  one could explain the non detection of the SDW-

mediated superconductivity in  $(\text{TMTSF})_2\text{NO}_3$ . The maxima of the Lindhard response nicely account for the modulation wave vector experimentally determined by NMR in the SDW ground state of these salts. It is noteworthy that the strength of the AO gap in the  $(\text{TMTSF})_2\text{ClO}_4$  and  $(\text{TMTSF})_2\text{NO}_3$  salts does not correlate with the decrease of the maximum response intensity because the gap opening does not necessarily occurs in the region of the FS with the best nesting properties. Finally, our first-principles calculation of the Lindhard response of the X =  $\text{ClO}_4$  and  $\text{NO}_3$  salts reveals 3D effects at low temperature which are considerably more difficult to model in analytical approaches. In a more general vein, this work and the accompanying one on  $(\text{TMTSF})_2\text{PF}_6$  [6] suggest that modern DFT approaches provide an accurate and unbiased tool to analyze the Lindhard response of low-dimensional molecular conductors which may be extremely useful when considering salts with complex crystal structures where analytical approaches are difficult.

## Acknowledgments

This work was supported by Spanish MINECO (the Severo Ochoa Centers of Excellence Program under Grants No. SEV-2017-0706 and SEV-2015-0496), Spanish MICIU, AEI and EU FEDER (Grants No. PGC2018-096955-B-C43 and No. PGC2018-096955-B-C44), Generalitat de Catalunya (Grant No. 2017SGR1506 and the CERCA Programme), and the European Union MaX Center of Excellence (EU-H2020 Grant No. 824143). We thank C. Bourbonnais, P. Foury-Leylekian, S. Tomic and W. Kang for useful discussions.

## References

- [1] Yamaji K, Ishiguro T and Saito G 1998 *Organic Superconductors* (2nd edition, Springer-Verlag, Berlin)
- [2] Lebed A (ed) 2008 *The Physics of Organic Superconductors and Conductors* (Springer, Berlin, Heidelberg)
- [3] Giamarchi T 2004 *Chem. Rev.* **104** 5037–5056
- [4] Bourbonnais C and Jérôme D 2008 Interacting electrons in quasi-one-dimensional organic superconductors *The Physics of Organic Superconductors and Conductors* ed Lebed A (Springer, Berlin Heidelberg) p 357–412
- [5] Bourbonnais C 1990 Antiferromagnetism and superconductivity in organic conductors *Current trends in the Physics of Materials* ed Chiarotti G F, Fumi F and Tosi M P (North Holland: Amsterdam) p 739–769
- [6] Guster B, Pruneda M, Ordejón P, Canadell E and Pouget J P 2020 *J. Phys. Condens. Matter* **32** 345701
- [7] Pashkin A, Dressel M, Hanfland M and Kuntscher C A 2010 *Phys. Rev. B* **81** 125109
- [8] Moser J, Gabay M, Auban-Senzier P, Jérôme D, Bechgaard K and Fabre J M 1998 *Eur. Phys. J. B* **16** 39–46
- [9] Dressel M, Petuhkov K, Salameh B, Zornoza P and Giamarchi T 2005 *Phys. Rev. B* **71** 075104

- [10] Jacobsen C S, Tanner D B and Bechgaard K 1983 *Phys. Rev. B* **28** 7019–7032
- [11] Henderson W, Vescoli V, Tran P, Degiorgi L and Gruner G 1999 *Eur. Phys. J. B* **11** 365–368
- [12] Jérôme D and Yonezawa S 2016 *C. R. Physique* **17** 357–375
- [13] Sedeki A, Bergeron D and Bourbonnais C 2012 *Phys. Rev. B* **85** 165129
- [14] Pouget J P and Ravy S 1996 *J. Physique I France* **6** 1501–1525
- [15] Jérôme D and Schulz H J 1982 *Adv. Phys.* **31** 299–490
- [16] Pouget J P, Shirane G, Bechgaard K and Fabre J M 1983 *Phys. Rev. B* **27** 5203–5206
- [17] Le Pévelen D, Gaultier J, Barrans Y, Chasseau D, Castet F and Ducasse L 2001 *Eur. Phys. J. B* **19** 363–373
- [18] Pouget J P, Moret R, Comès R and Bechgaard K 1981 *J. Physique Lett.* **42** L543–L546
- [19] Barrens Y, Gaultier J, Bracchetti S, Guionneau P, Chasseau D and Fabre J M 1999 *Synth. Met.* **103** 2042–2043
- [20] Tomic S, Jérôme D, Cooper J R and Bechgaard K 1988 *Synth. Met.* **27** B645–B649
- [21] Nagai Y, Nakamura H and Machida M 2011 *Phys. Rev. B* **83** 104523
- [22] Alemany P, Pouget J P and Canadell E 2014 *Phys. Rev. B* **89** 155124
- [23] Aizawa H and Kuroki K 2018 *Phys. Rev. B* **97** 104507
- [24] Hohenberg P and Kohn W 1964 *Phys. Rev.* **136** B864–B871
- [25] Kohn W and Sham L J 1965 *Phys. Rev.* **140** A1133–A1138
- [26] Soler J M, Artacho E, Gale J D, García A, Junquera J, Ordejón P and Sánchez-Portal D 2002 *J. Phys.: Condens. Matter* **14** 2745–2779
- [27] Artacho E, Anglada E, Diéguez O, Gale J D, García A, Junquera J, Martin R M, Ordejón P, Pruneda J M, Sánchez-Portal D and Soler J M 2008 *J. Phys.: Condens. Matter* **20** 064208
- [28] Perdew J P, Burke K and Ernzerhof M 1996 *Phys. Rev. Lett.* **77** 3865–3868
- [29] Troullier N and Martins J L 1991 *Phys. Rev. B* **43** 1993–2006
- [30] Kleinman L and Bylander D M 1982 *Phys. Rev. Lett.* **48** 1425–1428
- [31] Louie S G, Froyen S and Cohen M L 1982 *Phys. Rev. B* **26** 1738–1742
- [32] Artacho E, Sánchez-Portal D, Ordejón P, García A and Soler J M 1999 *Phys. Stat. Solidi (b)* **215** 809–817
- [33] Monkhorst H J and Pack J D 1976 *Phys. Rev. B* **13** 5188–5192
- [34] Le Pévelen, D 1999, Ph. D. thesis, Université de Bordeaux I.
- [35] Hebrard-Brachetti, S 1996, Ph. D. thesis, Université de Bordeaux I.
- [36] Ziman J M 1972 *Principles of the Theory of Solids* (Cambridge University Press, Cambridge)
- [37] Johannes M D, Mazin I I and Howells C A 2006 *Phys. Rev. B* **73** 205102
- [38] Heil C, Sormann H, Boeri L, Aichhorn M and von der Linden W 2014 *Phys. Rev. B* **90** 115143
- [39] Divilov S, Mayo S G, Soler J M and Yndurain F arXiv:2007.04737v1 [cond-mat.mtrl-sci], 9 Jul 2020.
- [40] Guster B, Pruneda M, Ordejón P, Canadell E and Pouget J P 2019 *Phys. Rev. Materials* **3** 055001
- [41] Pouget J P, Moret R, Comès R, Bechgaard K, Fabre J M and Giral L 1982 *Mol. Cryst. Liq. Cryst.* **79** 485–499
- [42] Hasegawa Y and Kishigi K 2008 *Phys. Rev. B* **78** 045117
- [43] Delrieu J M, Roger M, Coulon C, Laversanne R and Dupart E 1988 *Synth. Met.* **27** 35–40
- [44] Roger M, Delrieu J M and Mbougue E W 1986 *Phys. Rev. B* **34** 4952–4955
- [45] Hiraki K, Nemoto T, Takahashi T, Kang H, Jo Y J, Kang W and Chung O H 2003 *Synth. Met.* **135-136** 691–692
- [46] Satsukawa H, Hiraki K, Takahashi T, Kang H, Jo Y I and Kang W 2004 *J. Phys. IV France* **114** 133–134
- [47] Wzietek P, Creuzet F, Bourbonnais C, Jérôme D, Bechgaard K and Batail P 1993 *J. Physique I France* **3** 171–201
- [48] Pouget J P 2012 *Crystals* **2** 466–520
- [49] Pouget J P, Moret R, Comès R, Shirane G, Bechgaard K and Fabre J M 1983 *J. Phys. IV Colloques* **44** C3–969
- [50] Cao N, Timusk T and Bechgaard K 1996 *J. Phys. I France* **6** 1719–1726
- [51] Mazaud, A 1981, M. Sc. thesis, Université de Paris-Sud.
- [52] Moret R, Pouget J P, Comès R and Bechgaard K 1982 *Phys. Rev. Lett.* **49** 1008–1012
- [53] Pouget J P, Alemany P and Canadell E 2018 *Mater. Horizons* **5** 590–640
- [54] Bruisma R and Emery V J 1983 *J. Phys. IV Colloques* **44** C3–1115